




Role of Topocentric Parallax in Near-Earth Object Initial Orbit Determination

Chengxing Zhai¹ , Michael Shao¹, Navtej S. Saini¹, Philip Choi², Russell Trahan¹, Kutay Nazli², Max Zhan¹, and Nez Evans²
¹Jet Propulsion Laboratory, California Institute of Technology, 4800 Oak Grove Dr, Pasadena, CA 91109, USA; chengxing.zhai@jpl.nasa.gov
²Pomona College, Claremont, CA 91109, USA

Received 2021 November 8; accepted 2021 December 15; published 2022 January 31

Abstract

Near-Earth Object (NEO) initial orbit determination typically uses astrometric measurements during a close approach over a time window much shorter than the orbital period of the NEO. The initial orbit is only weakly determined with dominant uncertainties in the distance of the NEO from the Earth. Topocentric astrometric measurements allow us to estimate NEO distances using observed nonlinear motions of the NEOs relative to observers, which come from the relative orbital motion of the NEOs to the Earth plus the topocentric parallax (parallax) from the diversity of observatory locations relative to the Earth center. We calculate the ratio of the contributions to the nonlinear motion from the relative orbital motion and the parallax to be approximately $(T\Delta/(\text{day au}))^2$, where T is the arc length measured in days and Δ is the distance of close approach. The dominant nonlinear motion for ranging the NEO comes from the relative orbital motion of the NEO to the Earth center, due to mainly the differential solar gravitational acceleration, when $T\Delta \gtrsim 1$ day au and the parallax when $T\Delta \lesssim 1$ day au. This is confirmed by simulation data and supported by observational data of real NEOs. In the regime $T\Delta \lesssim 1$ day au, the orbit determination uncertainties are inversely proportional to the amplitude of the parallax. Introducing diversities of hour angles and observatory latitudes (especially alternating between extreme values) into scheduled follow-up observations can improve the parallax amplitude, thus the orbit accuracy. Most of the newly discovered NEOs are in this regime, we recommend optimizing parallax by properly scheduling observations when the NEO is very close to the Earth and using synthetic tracking to improve astrometry accuracy for initial orbit determination.

Key words: Near-Earth objects – Orbit determination – Parallax

1. Introduction

NASA's near-Earth object (NEO) observation program is actively surveying NEOs to find asteroids greater or equal to 140 m ($H \lesssim 22$) with 90% completeness to fulfill the extended congressional mandate for planetary defense.³ The NEO observation program also aims at inventorying all the NEOs that could support NASA's exploration goals or pose an impact threat. NEOs are usually discovered during close approach to the Earth with sufficient apparent brightness. Upon detection and during the same close approach, we need astrometric follow-up measurements to determine an initial orbit well enough for the NEO (1) to find whether it is a potentially hazardous asteroid (PHA) by estimating the probability for it to impact the Earth, (2) to track the NEO if it is a PHA or NASA's potential target for future exploration, and (3) to recover the NEO at its next apparition. The Minor Planet Center (MPC), which archives all the NEO measurements, announces a NEO discovery and assigns the NEO a provisional designation via a Minor Planet Electronic Circular (MPEC) if sufficient

consistent measurements are available for the NEO (Veres et al. 2018).

Currently, the surveys are discovering about 3000 new NEOs per year, and this rate has been increasing steadily (https://cneos.jpl.nasa.gov/stats/site_all.html) with the major players being the Catalina Sky Survey (CSS) (Christensen 2019), the Panoramic Survey Telescope and Rapid Response System (Pan-STARRS) (Kaiser et al. 2002), and the Asteroid Terrestrial-impact Last Alert System (ATLAS) (Tonry et al. 2018). The Zwicky Transit Facility (ZTF) (Bellm et al. 2019) with a gigantic FOV and a machine-learning-based streak detection (Duvet et al. 2019; Ye et al. 2019) also started to regularly discover NEOs, including very fast-moving NEOs detected as streaks. With the development of the synthetic tracking (ST) technique (Shao et al. 2014; Zhai et al. 2014; Heinze et al. 2015), we expect more small NEOs to be discovered by avoiding the trailing loss. The majority of the newly discovered NEOs are smaller than 100 m with a limited time window for follow-up observations. Future surveys like the Large Synoptic Survey Telescope (LSST) (Ivezić et al. 2019) and space missions like the NEO Surveyor Mission (Mainzer et al. 2015) will add significantly more new detections. Therefore, efficiently performing timely follow-up

³ <https://www.congress.gov/109/crpt/hrpt158/CRPT-109hrpt158.pdf>

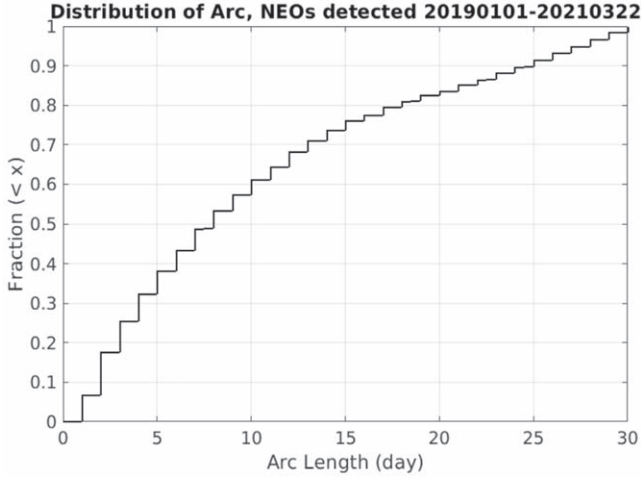


Figure 1. Distribution of arc ($T \leq 30$ day) for 4246 NEOs detected in 2019 January–2021 March according to MPC (<https://minorplanetcenter.net/iau/lists/LastUnusual.html>).

observations of new objects presents a challenge to the NEO community.

As NASA’s NEO program shifts from surveying 1 km size NEOs to smaller asteroids, the time window for most of the follow-up observations does not exceed 30 days. For example, according to MPC (<https://minorplanetcenter.net/iau/lists/LastUnusual.html>), about 75% of the one-opposition unnumbered objects detected in 2019 January–2021 March have arc length no more than 30 days. Figure 1 displays the distribution of the arc length for these 4246 objects with no more than a 30 day arc. Greater than 50% of NEOs have arc length less than 8 days, and about 25% of NEOs have arc length less than 3 days.

This accuracy of the initial orbit directly affects how easy the NEO can be recovered at its next apparition (Roa et al. 2020). Because the initial NEO orbit is estimated using astrometric measurements over an arc much shorter than the orbital period, the orbit is only weakly determined with one or two-dimensions having large uncertainties due to the poorly determined NEO distance (Milani et al. 2005, 2008). The NEO distance is determined using nonlinear motion between the NEO and the observatories, which includes both the nonlinear orbital motion of the NEO relative to the Earth and the change of locations of the observatories relative to the Earth center. The nonlinear NEO orbital motion relative to the Earth center mainly comes from the differential solar gravitational acceleration (DSGA). The change of locations of the observatories relative to the Earth center introduces topocentric parallax. Traditional wisdom to improve orbit accuracy is to extend the arc length to increase the signal of DSGA. However, for small NEOs, this approach is limited by the apparent brightness of the NEO. This motivates us to study the role of topocentric parallax, from the diversity of the locations of observatories relative to the Earth center, in NEO orbit determination using

topocentric astrometric measurements. Topocentric parallax (parallax) can be from the rotation of the Earth of a single observatory or observations from multiple observatories. This effect from the change of the position of an observatory has been discussed in comparing Gauss’s and Laplace’s methods for orbit determination (Poincare 1906; Milani et al. 2008) to show parallax could not be approximated by a simple quadratic expansion in time because of its short timescale of variation. Veres et al. (2014) have also studied the effect of parallax from two observatories for determining the probability of a NEO to impact the Earth. However, so far, there is no systematic study of the effect of parallax on the NEO initial orbit determination.

Here we report our study to address (1) when the parallax is important for NEO orbit determination and (2) how to schedule observations to increase the parallax to improve orbit accuracy. In the next section, we formulate the NEO orbit determination to introduce notations and perform a semi-quantitative analysis to show the two regimes of orbit determination depending on whether parallax or the DSGA contributes mainly the nonlinear motion for the NEO distance determination. In Section 3, we first confirm the two regimes for NEO orbit determination using simulation and actual NEO observational data. We then present parallax effects in NEO determination from Earth rotation and multiple observatories, and how scheduling can affect parallax amplitudes, and thus accuracy of orbit. Finally, we conclude and discuss the application of this study. The Appendix provides detailed derivations for Section 2.

2. NEO Orbit Determination using Astrometric Measurements from One Close Approach

Astrometric measurements provide the sky positions of a NEO, which we represent as unit vectors from the observer, at position \mathbf{P} with respect to the center of the Earth \mathbf{q}_e , to the NEO at \mathbf{r} in a heliocentric coordinate system as shown in Figure 2. We follow the notation of Milani et al. (2008) to use boldface to represent a vector in 3-d space, the lower case as its magnitude, and a hat on a vector for the unit vector pointing along the vector. For example, $\mathbf{q}_e = q_e \hat{\mathbf{q}}_e$ with q_e being the magnitude of \mathbf{q}_e and $\hat{\mathbf{q}}_e$ being its unit vector. Let $\boldsymbol{\rho}$ be the vector from the observer to the NEO and $\boldsymbol{\rho}_e$ be the vector from the center of the Earth to the NEO. We have

$$\begin{aligned} \boldsymbol{\rho}(t) &= \mathbf{r}(t) - \mathbf{q}_e(t) - \mathbf{P}(t), \quad \boldsymbol{\rho}_e(t) \\ &= \mathbf{r}(t) - \mathbf{q}_e(t) = \boldsymbol{\rho}(t) + \mathbf{P}(t), \end{aligned} \quad (1)$$

where we have explicitly included the dependency of time t .

Astrometric measurements give the constraints $\hat{\boldsymbol{\rho}}(t_i) = \hat{\boldsymbol{\rho}}_i$ with the unit vector $\hat{\boldsymbol{\rho}}_i$ representing the i th astrometric measurement taken at time t_i , which can be expressed as cross products,

$$\hat{\boldsymbol{\rho}}_i \times \boldsymbol{\rho}(t_i) = 0, \quad i = 1, 2, \dots, N_{\text{obs}}, \quad (2)$$

where N_{obs} is the total number of observations. In general, Equation (2) allows us to determine the six orbital parameters,

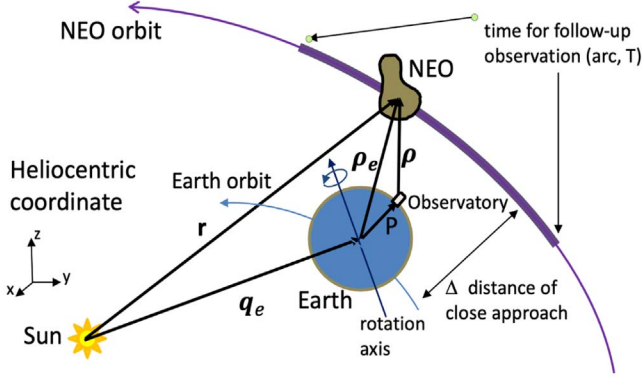


Figure 2. Schematics (not in proportion) showing observation of a NEO during its close approach.

in which we parameterize $\rho(t)$. We need at least three astrometric observations, $N_{\text{obs}} \geq 3$, to fully determine an orbit because each of the astrometric equations provides two independent constraints.

2.1. Weakly Determined NEO Orbit

We are interested in the NEO orbit determination with an arc ($T \leq 30$ days) much less than the orbital period of order ~ 1 yr. It is a good approximation to expand vector $\rho_e(t)$ in a Taylor series around some reference time t_0 chosen in the mid of the range of t_i 's to have

$$\rho(t) \approx \rho_e(t_0) + \dot{\rho}_e(t_0)(t - t_0) + \frac{1}{2}\ddot{\rho}_e(t_0)(t - t_0)^2 - \mathbf{P}(t). \quad (3)$$

where we only kept through the quadratic term as in the classical methods by Gauss and Laplace. This is appropriate because keeping only the linear term is insufficient to determine all the six orbital parameters, and including an extra quadratic term would allow us to do so. Note that we did not do this expansion for $\rho(t)$ because $\mathbf{P}(t)$ varies with a period of 1 day or could be discontinuous in time if multiple observatories are involved, therefore a Taylor expansion would not be a good expansion (Poincare 1906; Marchi et al. 2004; Milani et al. 2008). Because the Earth's ephemeris is well determined, once we know $\rho_e(t_0)$ and $\dot{\rho}_e(t_0)$, we have the 3d position and velocity of the NEO at time t_0 in a heliocentric coordinate system, which means that we fully determine the NEO's orbit. Thus, the orbit determination may be viewed as determining $\rho_e(t_0)$ and $\dot{\rho}_e(t_0)$ using Equations (2) and (3).

We now examine the typical magnitudes of the terms in the expression (3) of $\rho(t)$ for $T \leq 30$ days. The semimajor axis of a NEO orbit is ~ 1 au with a period ~ 1 yr, thus the first term $\rho_e(t_0)$ is of order 1 au, the linear motion over ± 15 days is $\sim (2\pi)15 \text{ day}/1 \text{ yr} \sim 0.26$ au, the acceleration term $\sim 1/2 (15 \text{ day}(2\pi/1 \text{ yr}))^2 \sim 0.033$ au, and the position of observatory

relative to the center of the Earth $\mathbf{P}(t)$, whose variation gives the parallax, is of order of the Earth radius $R_e \sim 4.2e-5$ au.

It is attractive to consider solving for $\rho_e(t_0)$, $\dot{\rho}_e(t_0)$ by keeping only the first two terms

$$\rho(t) \approx \rho_e(t_0) + \dot{\rho}_e(t_0)(t - t_0) \quad (4)$$

in Equation (3). However, this is not possible because we can not determine the overall scale, or the distance of the NEO, by using just the astrometric measurements $\rho(t_i)$'s. Physically, the astrometric measurements do not carry the dimension of length, thus are invariant under the transform $\rho_e(t_0)$, $\dot{\rho}_e(t_0) \rightarrow \xi\rho_e(t_0)$, $\xi\dot{\rho}_e(t_0)$ according to Equation (4). This means that if $\rho_e(t_0)$, $\dot{\rho}_e(t_0)$ is a solution, $\xi\rho_e(t_0)$, $\xi\dot{\rho}_e(t_0)$ is also valid solution where ξ is an arbitrary factor.

We now examine this in some detail. Following (Danby 1988; Milani et al. 2008), we define a right-handed orthonormal basis ($\hat{\rho}_e$, $\hat{\mathbf{v}}$, $\hat{\mathbf{n}}$) using the unit vector $\hat{\rho}_e(t_0)$ and the first derivative $\dot{\hat{\rho}}_e(t_0)$ as

$$\eta \equiv |\dot{\hat{\rho}}_e(t_0)|, \hat{\mathbf{v}} \equiv \dot{\hat{\rho}}_e(t_0)/\eta, \hat{\mathbf{n}} \equiv \hat{\rho}_e(t_0) \times \hat{\mathbf{v}}, \quad (5)$$

and obtain the following kinematic relations (see Appendix for the detailed derivations)

$$\ddot{\hat{\rho}}_e = -\eta^2\hat{\rho}_e + \dot{\eta}\hat{\mathbf{v}} + \kappa\eta^2\hat{\mathbf{n}}, \quad (6)$$

$$\ddot{\rho}_e(t_0) = (\ddot{\rho}_e(t_0) - \eta^2)\hat{\rho}_e(t_0) + (2\dot{\rho}_e\eta + \rho_e\dot{\eta})\hat{\mathbf{v}} + \kappa\eta^2\rho\hat{\mathbf{n}}. \quad (7)$$

With three or more astrometric measurements $\hat{\rho}_i$'s at different epochs t_i 's, we can estimate the direction $\hat{\rho}_e(t_0)$, rate $\dot{\hat{\rho}}_e(t_0)$, and acceleration $\ddot{\hat{\rho}}_e(t_0)$ by approximating $\hat{\rho}_e(t)$ as a quadratic function of time, and then get η , $\dot{\eta}$ respectively using Equations (5) and (6). In case of a linear motion (4), $\ddot{\rho}_e = 0$. Using Equation (7) gives $\kappa = 0$ and $2\dot{\rho}_e\eta + \rho_e\dot{\eta} = 0$. We get $\dot{\rho}_e/\rho_e = -\dot{\eta}/(2\eta)$. Now we have just shown that we can estimate $\hat{\rho}_e$, $\hat{\mathbf{v}}$, η , and $\dot{\rho}_e/\rho_e$, missing only an overall scale ρ_e to fully determine $(\rho_e, \dot{\rho}_e)$ as $\rho_e = \rho_e\hat{\rho}_e$ and $\dot{\rho}_e = \rho_e(\eta\hat{\mathbf{v}} + \dot{\rho}_e/\rho_e\hat{\rho}_e)$.

To summarize, with a linear motion approximation, we can estimate the 2d sky position $\hat{\rho}_e$ of NEO at t_0 , the 2d sky rate $\eta\hat{\mathbf{v}}$ at t_0 , and the relative radial velocity $\dot{\rho}_e/\rho_e$. We have one weakly determined parameter ρ_e because it can only be estimated by including higher-order terms in the expansion (3), *i.e.* we need to measure astrometric signal beyond the term linear with time to get the distance of the NEO ρ_e . This is consistent with that both Gauss and Laplace methods use a dynamical equation to determine the NEO distance. The high uncertainties along this dimension have been discussed by Milani et al. (2008). We note that in case η is small, the uncertainty in $\dot{\rho}_e/\rho_e$ grows as $\sim 1/\eta$. For very small η , we eventually need to also use the higher-order nonlinear motion to determine the relative radial velocity $\dot{\rho}_e/\rho_e$. These are the uncommon cases where we have two weakly determined dimensions.

2.2. Two Regimes to Determine the NEO Distance

In the previous subsection, we found that the NEO distance is determined by the astrometric signal of the motion of NEO relative to the observer that is nonlinear in time. As a NEO gets close to the Earth, the DSGA between the NEO and the Earth decreases. Therefore, the parallax becomes significant. In this subsection, we will consider the astrometric measurements from a NEO close approach and study the two regimes for the dominant nonlinear motion to determine the NEO distance being the DSGA and the parallax respectively.

The astrometric signal comes mainly from the component transverse to the $\hat{\rho}_e$, which we use notation $[\mathbf{V}]_{\perp} \equiv \mathbf{V} - \hat{\rho}_e(\mathbf{V} \cdot \hat{\rho}_e)$ to denote the component of a vector \mathbf{V} that is perpendicular to $\hat{\rho}_e(t_0)$. Therefore, the relevant component of Equation (3) is

$$[\rho(t)_{\text{nonlin}}]_{\perp} \approx \frac{1}{2}[\ddot{\rho}_e(t_0)]_{\perp}(t - t_0)^2 - [\mathbf{P}(t)_{\text{nonlin}}]_{\perp}, \quad (8)$$

where we use subscript *nonlin* to denote the portion of the time dependency that is nonlinear with time t . The accelerations of the NEO and the Earth in a heliocentric inertia frame are dominated by the solar gravitational force. To the leading order, we ignore the gravitational force of planets and moons.⁴ By Newton's law, we have DSGA to be

$$\begin{aligned} \ddot{\rho}_e &= -\mu \left(\frac{\mathbf{r}}{r^3} - \frac{\mathbf{q}_e}{q_e^3} \right) \\ &= -\mu \left[\frac{\mathbf{q}_e + \rho_e}{(q_e^2 + 2\mathbf{q}_e \cdot \rho_e + \rho_e^2)^{3/2}} - \frac{\mathbf{q}_e}{q_e^3} \right] \end{aligned} \quad (9)$$

where μ is the product of the solar mass and Newton's gravitational constant. NEO observations are mainly performed when the NEO is close to the Earth, therefore, $\rho \sim \rho_e \ll q_e \sim 1$ au. We expand the acceleration in powers of ρ_e/q_e to the second order and only consider the component transverse to ρ_e , as derived in [Appendix](#) to get

$$\begin{aligned} [\ddot{\rho}_e(t_0)]_{\perp} &\approx 3\mu \left[\frac{(\rho_e(t_0) \cdot \hat{\mathbf{q}}_e(t_0))}{q_e(t_0)^3} \right. \\ &\quad \left. + \frac{\rho_e(t_0)^2 - 5(\hat{\mathbf{q}}_e(t_0) \cdot \rho_e(t_0))^2}{2q_e(t_0)^4} \right] [\hat{\mathbf{q}}_e(t_0)]_{\perp}. \end{aligned} \quad (10)$$

Inserting Equation (10) into Equation (8) gives

$$\begin{aligned} [\rho(t)_{\text{nonlin}}]_{\perp} &\approx \frac{3\mu(t - t_0)^2}{2} \left[\frac{(\rho_e \cdot \hat{\mathbf{q}}_e)}{q_e^3} + \frac{\rho_e^2 - 5(\hat{\mathbf{q}}_e \cdot \rho_e)^2}{2q_e^4} \right] \\ &\quad \times [\hat{\mathbf{q}}_e]_{\perp} - [\mathbf{P}(t)_{\text{nonlin}}]_{\perp} \end{aligned} \quad (11)$$

⁴ However, when a NEO gets close to the Earth within ~ 0.01 au, the Earth's gravitational force would need to be included. We will not consider this case and defer it as a future study.

where we have dropped the explicit time argument t_0 for q_e , ρ_e , and $\hat{\mathbf{q}}_e$ to make the formula simpler. The first term in the square bracket in Equation (11) is linear with $\rho_e(t_0)$ and would not allow us to determine the ρ_e because it scales the same way as the linear motion terms under the transform $\rho_e(t_0), \dot{\rho}_e(t_0) \rightarrow \xi\rho_e(t_0), \xi\dot{\rho}_e(t_0)$ to preserve the astrometric measurements. Therefore, the leading order term from DSGA that allows us to estimate ρ_e is quadratic in ρ_e , *i.e.* the second term in the square bracket in Equation (11). Assume t_0 is at the center of the observation arc, the quadratic function $(t - t_0)^2$ has the peak value of $T^2/4$ and the valley value of 0. Therefore, the astrometric signal from DSGA has a quadratic time dependency with a peak-to-valley amplitude of

$$\text{DSGA} \sim \frac{3\mu T^2 \Delta^2 |1 - 5 \cos \theta_e| \sin \theta_e}{8q_e^4}, \quad (12)$$

where θ_e is the angle between $\hat{\mathbf{q}}_e$ and $\hat{\rho}_e$ and we have used $\hat{\mathbf{q}}_e \cdot \rho_e = \rho_e \cos \theta_e$, $|\hat{\mathbf{q}}_e]_{\perp}| = \sin \theta_e$, and $\rho_e \sim \Delta$, the distance of close approach.

We now consider the relative importance of the DSGA and the parallax term in Equation (11) for determining the distance ρ_e . Parallax comes from the variation of $\mathbf{P}(t)$ with a period of 1 day, therefore, unless there is no diversity of observatory locations and hour angles, a significant nonlinear motion should exist. The peak-to-valley variation $P(t)$ is approximately twice the Earth Radius R_e at maximum.⁵ The ratio of the DSGA and the parallax is

$$\begin{aligned} \frac{\text{DSGA}}{\text{Parallax}} &\sim \frac{3\mu T^2 \Delta^2 |1 - 5 \cos \theta_e| \sin \theta_e}{16q_e^4 R_e} \\ &\sim \frac{0.15\mu T^2 \Delta^2}{q_e^4 R_e} \sim \left(\frac{T\Delta}{\text{day au}} \right)^2, \end{aligned} \quad (13)$$

where we have computed the average of $|1 - 5 \cos \theta_e| \sin \theta_e$ over $[0, 90]$ deg to be approximately 0.8. The acceleration term grows quadratically with the arc length. This term is also quadratic in $\rho_e(t_0)$, thus smaller for a closer approach. To the first order, the ratio $T\Delta/(\text{day au})$ determines the relative importance of DSGA to the parallax, which allows us to specify two regimes of orbit determination sensitivity: for $T\Delta \gtrsim 1$ day au, the DSGA dominates the orbit determination for estimating the NEO distance and for $T\Delta \lesssim 1$ day au, parallax dominates. In general, for a small NEO, both arc T and Δ tend to be small, therefore, the parallax dominates its initial orbit determination. This is confirmed by simulation and orbit sensitivity study using observational data as presented in [Section 3.2](#).

⁵ Practically, we cannot reach this maximum due to airmass constraint as well as the latitudes of the observatories.

2.3. Topocentric Parallax and a Measure of its Amplitude

Parallax can be introduced by the Earth rotation for observations from a single observatory at different epochs (different hour angles) as well as observations from different observatories at different latitudes. Parallax from diversities of hour angles and observatory latitudes can be combined and quantified by vector $[\mathbf{P}(t)]_{\perp}$. In deriving Equation (13), for convenience, we considered the peak-to-valley amplitude of the nonlinear signal. For orbit determination using observations at t_i 's, only the nonlinear signals sampled at the observation times t_i 's are relevant. Because a motion linear in time can be described by Equation (4), which does not help determine the NEO distance, we obtain the nonlinear portion of motion by detrending a linear motion

$$[\mathbf{P}(t)_{\text{nonlin}}]_{\perp} = \mathbf{P}_{\perp}(t) - \boldsymbol{\alpha} - \boldsymbol{\beta}t, \quad (14)$$

where vectors $\boldsymbol{\alpha} \equiv (\alpha^1, \alpha^2, \alpha^3)$ and $\boldsymbol{\beta} \equiv (\beta^1, \beta^2, \beta^3)$ represent 3d vector coefficients determined by a linear fitting to the three components of 3d vector $\mathbf{P}_{\perp}(t_i)^j$ by requiring

$$(\boldsymbol{\alpha}, \boldsymbol{\beta}) = \arg \min_{\boldsymbol{\alpha}^j, \boldsymbol{\beta}^j} \sum_{i=1}^{N_{\text{obs}}} \sum_{j=1}^3 |\mathbf{P}_{\perp}(t_i)^j - \alpha^j - \beta^j t_i|^2. \quad (15)$$

We use the rms (root-mean-squares) of the nonlinear motion as a measure of the parallax amplitude in units of Earth radius,

$$\Pi_{\text{tot}} \equiv \frac{1}{R_e} \sqrt{\frac{1}{N_{\text{obs}}} \sum_{i=1}^{N_{\text{obs}}} \sum_{j=1}^3 |[\mathbf{P}(t_i)_{\text{nonlin}}]_{\perp}^j|^2}, \quad (16)$$

We will show in Section 3.3 that the orbit uncertainties are inversely proportional to the parallax as defined by Equation (16) in the regime when parallax dominates the NEO orbit determination.

Note that our derivation was for the case of a close approach with Δ much smaller than 1 au. When Δ is comparable with 1 au, in general, the nonlinear relative orbital motion of a minor planet relative the Earth over 1 day is of scale $\sim 1/2(2\pi)(0.5 \text{ day}/1\text{yr})^2 1\text{au} \sim 5.6e3 \text{ km}$, $\sim 0.87R_e$ comparable with parallax. When $T \geq 2 \text{ day}$, the nonlinear relative orbital motion is in general larger than the parallax signal. Bernstein & Kushalani 2000 found that the parallax is too small for determining orbits of Kuiper Belt objects requiring longer arcs to gain nonlinear signal from relative orbital motion. However, if the observations are performed near opposition (a preferred situation for target brightness), the nonlinear orbital motion from DSGA is approximately along the direction of observation $\boldsymbol{\rho}_e$, so we have $\sin \theta_e \ll 1$ in Equation (12) and the parallax would dominate. This is the case studied by Metchev (2015), Lin et al. (2016) to use parallax to determine the distance of the main belt asteroids using observations over only 2 nights.

3. Parallax Effect in Orbit Determination

3.1. Estimate Orbit Determination Uncertainties using Simulation

We use simulation to study the effect of parallax in NEO orbit determination. We generate NEO orbits using Granvik's NEO orbit database (Granvik et al. 2016), which contains 731,683 synthetic NEOs down to an $H < 25 \text{ mag}$. Figure 3 shows the distributions of the six orbital parameters. The distributions are almost statistically independent from each other except for the semimajor axis and the eccentricity, whose correlation is 0.513. This is expected because if the semimajor axis is large, the eccentricity needs to be large too for the NEO to get close to the Earth's orbit.

Because this is a sensitivity study, we ignore the gravitational forces from planets and moons compared with solar gravitational force and assume Keplerian orbits for all the NEOs and the Earth following (Buie et al. 2016). The positions of the NEOs and the Earth are used to simulate observational scenarios for the Pomona College's 1 m telescope at the Table Mountain Facility (code 654) observing these NEOs with a limiting magnitude of 21. We require the airmass less than 2, the elongation greater than 60° , and the arc length greater than 1 day and no more than 30 days.

NEO orbit determination can be viewed as a nonlinear least-squares fitting of $y_i = M(X, t_i)$, $i = 1, 2, \dots, 2N_{\text{obs}}$, where $M(X, t)$ is the astrometric measurement model, a function of orbital parameters $X = (a, e, i, \Omega, \omega, M_0)$ (representing respectively the semimajor axis, eccentricity, inclination, argument of ascending node, argument of perigee, and mean anomaly) and time t . y_i 's represent N_{obs} 2-d astrometric measurements taken at time t_i 's. For each close approach, we calculate the orbit determination uncertainty using a linear analysis to approximate the measurement model as a linear model:

$$\delta y_i = \sum_{j=1}^6 \frac{\partial M(X, t_i)}{\partial X_j} \bigg|_{X=X_0} \delta X_j = \sum_{j=1}^6 J_{ij} \delta X_j. \quad (17)$$

y represents the N_{obs} astrometric measurements and J is the Jacobian matrix (Fletcher 1987). A least-squares estimator gives

$$\delta \hat{X} = J^\dagger \delta y \quad (18)$$

where J^\dagger is the pseudo inverse (Luenberger 1969) of J . We derive the covariance matrix as

$$\text{Cov}(X) = \text{Cov}(\delta X) = J^\dagger \text{Cov}(\delta y) J^{\dagger T}. \quad (19)$$

Assuming the measurement errors are uncorrelated⁶ with an accuracy of ϵ , the covariance matrix $\text{Cov}(\delta y)$ is a diagonal matrix with elements ϵ^2 . Therefore, $\text{Cov}(X) = \epsilon^2 J^\dagger J^{\dagger T}$. Because we at least have six measurements, $J^\dagger = (J^T J)^{-1} J^T$, $\text{Cov}(X) = \epsilon^2 (J^T J)^{-1}$. With this, we can estimate orbit

⁶ A generalization to more complex measurement uncertainties represented as a covariance matrix is straightforward.

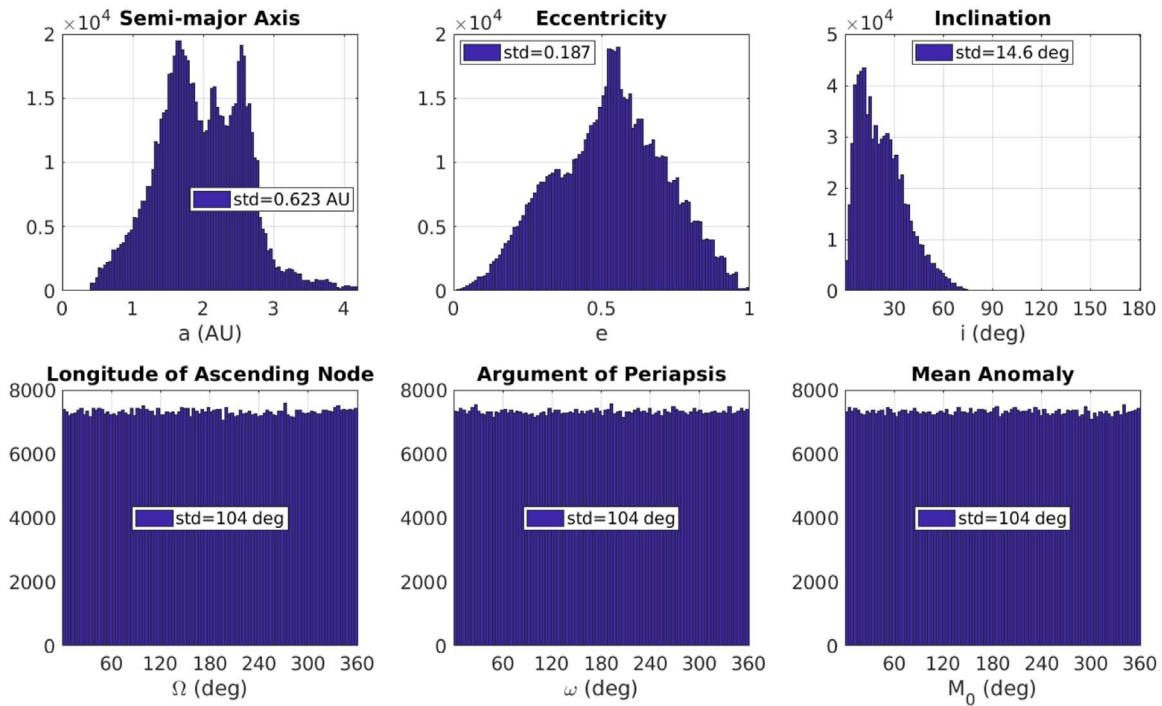


Figure 3. Histogram of orbital parameters from the Granvik's database.

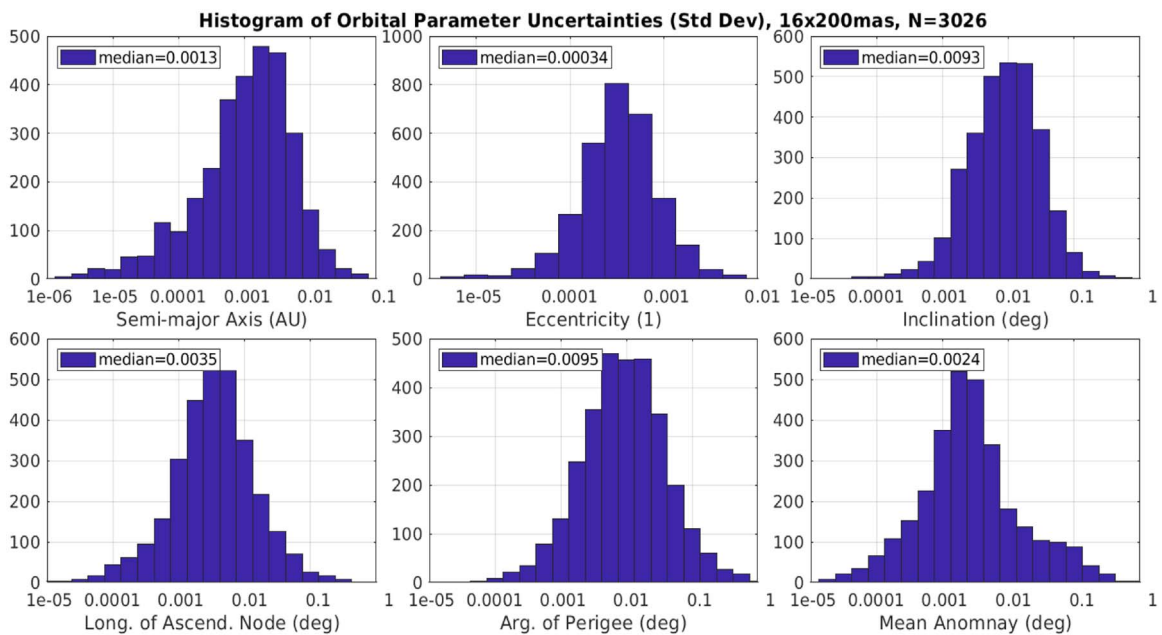


Figure 4. Histograms of the uncertainties of orbital parameters over 3026 NEO close approach scenarios.

uncertainties in terms of orbital parameter covariances for all the simulated observational scenarios. Figure 4 shows histograms of the standard deviations for each of the six orbital parameters using 16 astrometric measurements of accuracy of 200 mas. The

x -axis is displayed in log scales showing a large range of uncertainties depending on the simulated 3026 observation scenarios with arc length range 1–30 day and distance of close approach from 0.0025 au to 0.5 au.

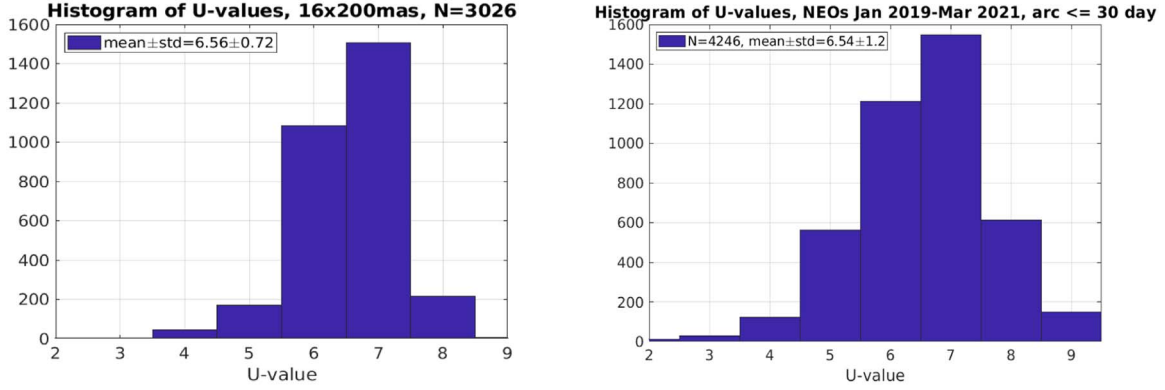


Figure 5. The left plot shows U -value histogram for the orbit derived using 16 astrometric observations of accuracy 200 mas. The right plot displays the distribution of U -values of the NEOs detected in Jan 2019-Mar 2021 with roughly the same mean value.

Because the orbit is weekly determined and the dominant error is in ranging the NEO, the uncertainties of the orbital parameters are highly correlated.

MPC uses the U -value (<https://minorplanetcenter.net/iau/info/UValue.html>) to quantify the orbit uncertainties. The U -value represents in-orbit longitude runoff on a logarithmic scale, closely related to how fast the uncertainties of predicted positions grow with time. It is straightforward to derive the distribution of the U -values using the uncertainties of the orbital parameters, which is displayed in the left plot in Figure 5 with a mean value of 6.56 and a standard deviation of 0.72. For comparison, the right plot shows the U -value histogram of NEOs that only have observations over one opposition from a query to the MPC database (<https://minorplanetcenter.net/iau/lists/LastUnusual.html>) of the one-opposition unnumbered objects discovered in 2019 January–2021 March. The mean value of 6.54 is very close to our simulation result for using 16 observations of 200 mas accuracy. These NEOs were observed with at least 3 tracklets (typically 12 observations, (Veres et al. 2018)) to get the provisional designations and usually with additional observations after getting the provisional designation. These NEOs typically have more than 16 measurements, indicating that most astrometric measurements are less accurate than 200 mas. Veres et al. 2017 reported that the best survey astrometry is from the PanSTARRS with an accuracy of ~ 120 mas for slowly moving objects. For fast moving-objects, this quickly degrades to 200 mas or higher values. Many survey astrometry is only accurate to ~ 500 mas. This diversity of astrometry accuracy probably explains the larger standard deviation of 1.2 in the right plot compared with the left plot. We note that even though the analysis by Veres et al. (2017) corrected the biases of the catalogs used using the method of Farnocchia et al. (2015), the uncorrected catalog errors could still render the reported astrometric errors slightly larger. It would be nice to quantify this error using the Gaia Catalog in the future.

3.2. Two Regimes for Determining NEO Distance

The NEO orbit determination is equivalent to determining the 3d position and velocity of the NEO at an epoch. In general, astrometric measurements do not directly provide ranging information, so the distance of the NEO from the observer is inferred from the nonlinear motion of the NEO relative to the observer(s). The nonlinear motion can be from the DSGA and the parallax. Their relative strength is approximately determined by the product of the arc T and the distance of close approach Δ as discussed in Section 2.2. We now use the simulation data to show when the parallax becomes important for NEO orbit determination when $T\Delta < 1$ day au.

To do this, we group close approach scenarios according to the arc length T and distances Δ and study orbit determination uncertainties as function of the arc length T and the distance of close approach Δ . Because the uncertainties of 6 orbital parameters are highly correlated. It is sufficient to show just the semimajor axis. We consider the NEOs coming close to the Earth with $\Delta < 0.5$ au. The top plots in Figure 6 show the median value of the standard deviations of the semimajor axis estimated using 6 (left) and 16 (right) astrometric observations of 20 mas accuracy from linear analyses of 3026 observation scenarios respectively in log scale. The red dash diagonal lines represent $T\Delta = 1$ day au, which separates two regimes of NEO orbit determination as discussed in Section 2.2. The top right is the regime where the nonlinear motion mainly comes from the relative acceleration of the NEO to the Earth in a heliocentric inertial frame. The uncertainties of the semimajor axis depend on the arc length T strongly. In the bottom left plot, the median value (blue with square marker) and values at top 10%, 5%, and 1% (dashed lines) are displayed as functions of T . The gray dashed line shows the $1/T^2$ behavior consistent with that the NEO distance is inferred using the nonlinear motion from the DSGA.

For $T\Delta \lesssim 1$ day au, the astrometric signal from parallax plays the dominant role in determining the NEO distance from

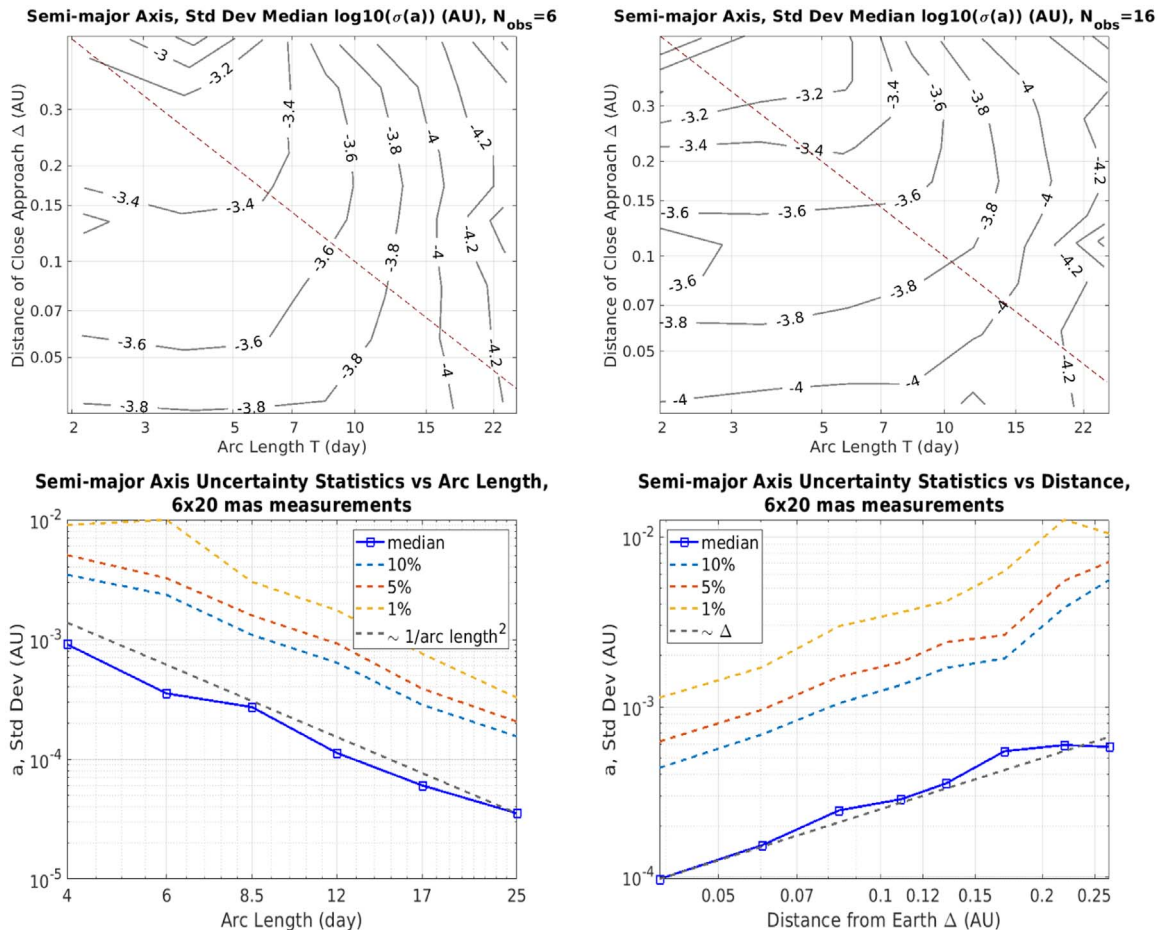


Figure 6. Top row: Contour plots showing the uncertainties of semimajor axis derived using 4 (left) and 16 (right) astrometric observations of accuracy 20 mas as a function of arc length T and distance of close approach Δ . Bottom row: left plot shows semimajor axis uncertainty depends on the arc length $\sim 1/T^2$ when in regime of $T\Delta > 1$ day au and the right plot shows semimajor axis uncertainty is proportional to the distance of approach when $T\Delta < 1$ day au.

the Earth.⁷ The right plot at the bottom of Figure 6 shows that the median and values at the top 10%, 5%, and 1% (dashed lines) depend linearly on the distance of close approach Δ as expected. This dependency shows that the closer the NEO gets to the Earth, the better sensitivity we have to determine the NEO orbit using the parallax.

The left plot in Figure 7 shows the dependency of U -values on the arc and distance of close approach, which has similar behavior to the semimajor axis. This is expected because the uncertainties of orbital parameters are highly correlated. Looking at the arc length dependency for cases of different distances of close-approach Δ , we can see that as arc length increases, the orbital accuracy improves weakly for $T\Delta < 1$ day au and significantly for $T\Delta > 1$ day au, where the DSGA dominates NEO orbit determination.

⁷ We randomly scheduled the observations as discussed in the next subsection, so the parallax signals are not maximized, only at an average level.

We validate our simulation by comparing statistics from the simulation study with the orbit determination statistics using NEO observation data from MPC. We downloaded data of six NEOs, 2021 CC₂, 2021 CV₃, 2021 CH₂, 2021 CG₃, 2021 CW₄, and 2021 CL₁₀ from the MPC’s Orbits/Observations Database. These recent discoveries were chosen because they have different distances of close approach and a sufficient number of observations allowing us to study the sensitivity to various arc lengths by using different subsets of measurements. We used the online *Find_Orb* tool provided by Project Pluto (<https://www.projectpluto.com/fo.htm>) to estimate orbital parameters of objects by inputting astrometric measurements in the MPC’s 80-Column format (<https://www.minorplanetcenter.net/iau/info/OpticalObs.html>). This allows us to estimate orbital parameters using actual NEO observation data to study orbit determination sensitivity. We obtain U -values as functions of the arc lengths of observations using 16 astrometric measurements covering different arc

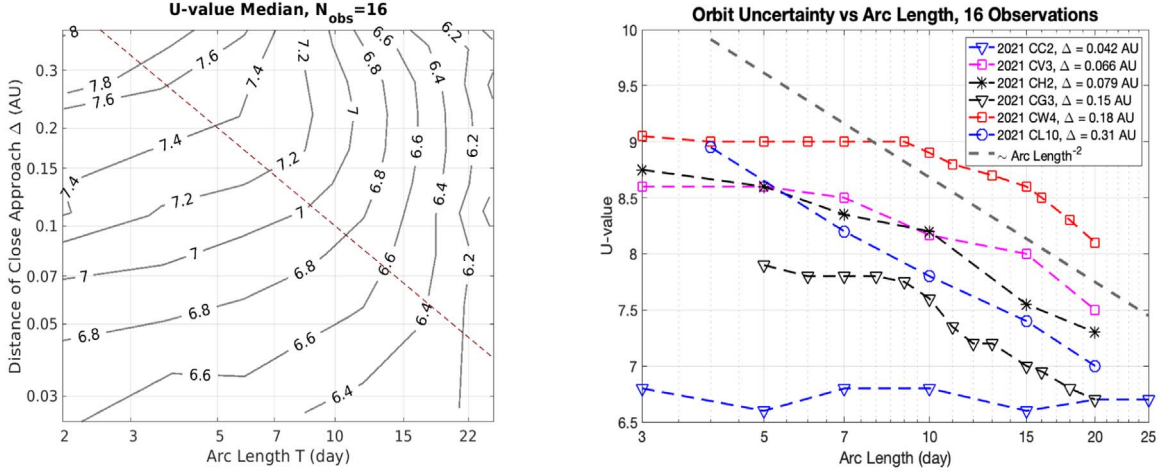


Figure 7. Left: U -value contour plots showing the orbit uncertainty derived from 16 astrometric measurements of accuracy 200 mas as function of arc length T and distance of close approach Δ . Right: Orbit uncertainty versus arc length of the observations using data from MPC and online findOrb.

lengths from subsetting the total amount of the available measurements.

We did not have enough data to generate a contour plot for U -value statistics but we can see the transition between the two regimes by examining the orbit accuracy as a function of the arc length. Here we clearly see that as the arc length gets long enough, the uncertainty decreases fast as $\sim 1/T^2$ for all the objects except for 2021 CC₂ in the regime where the orbit determination is dominated by the DSGA. For 2021 CC₂, $\Delta \sim 0.042$ au, our arc length range has not reached the value where the gravitational acceleration would be more important than the parallax, i.e., 2021 CC₂ is in regime $T\Delta \lesssim 1$ day au. For the shorter arc length side, the orbit uncertainties are much less sensitive to the arc length because the parallax dominates the orbit determination. The transition happens at $\sim (1\text{au}/\Delta)$ day as a first-order results. We note that this is an approximate result because it depends on the parallax amplitude of the observations and the specific observational geometry, e.g., the θ_e in Equation (13) in Section 2. Table 1 shows the parallax amplitudes for these objects computed using Equation (16). For example, the amplitude of parallax for 2021 CH₂ is weak, so we do not see the clear transition between the two regimes while this transition is clearer for larger amplitudes as for 2021 CG₃ and 2021 CW₄.

3.3. Parallax Dependency of Orbit Uncertainties

Because the regime $T\Delta \lesssim 1$ day au is important for NEOs with short arcs, we examine explicitly the relation between the orbit uncertainties and the parallax amplitude as defined by Equation (16) and study the orbit determination sensitivity to the scheduling of observations, which affects the parallax amplitudes. Topocentric parallax comes from the diversity of the observatory positions with respect to the center of the Earth

Table 1
Example Parallax amplitudes from 16 observations

Object Name	Distance Δ (au)	arc (day)	Parallax Amplitude
2021 CC ₂	0.042	3	0.41
2021 CV ₃	0.066	3	0.28
2021 CH ₂	0.079	3	0.10
2021 CG ₃	0.15	5	0.40
2021 CL ₁₀	0.18	4	0.16
2021 CW ₄	0.31	3	0.50

in an inertial reference frame. Observations from multiple observatories or a single observatory can measure parallax because the Earth rotates.

3.3.1. Parallax from a Single Observatory

As far as the observatory is not at the polar region, the Earth rotation can introduce topocentric parallax. Because the hour angle θ_{HA} of the observation represents the position of the observer relative to the center of the Earth when observing the NEO (see the left plot in Figure 8), the parallax amplitude can be expressed in terms of θ_{HA} as $\Pi_{\text{tot}} = \cos(\theta_{\text{lat}})\Pi_{\text{HA}}$, where θ_{lat} is the latitude of the observatory (~ 34 deg for TMO 654) and

$$\Pi_{\text{HA}} \equiv \sqrt{\frac{1}{N_{\text{obs}}} \min_{\alpha, \beta} \sum_i [\sin \theta_{\text{HA}}(t_i) - \alpha - \beta t_i]^2}, \quad (20)$$

where α and β are determined by a linear fit to minimize the rms of the residuals and t_i are the epochs of observations. In view of Equation (20), we would like to maximize $\sin \theta_{\text{HA}}(t_i)$ that is not linear with t_i and this is sensitive to the actual scheduling of the observations, i.e. the choice of t_i 's. To illustrate this, if we schedule NEO observations on three nights

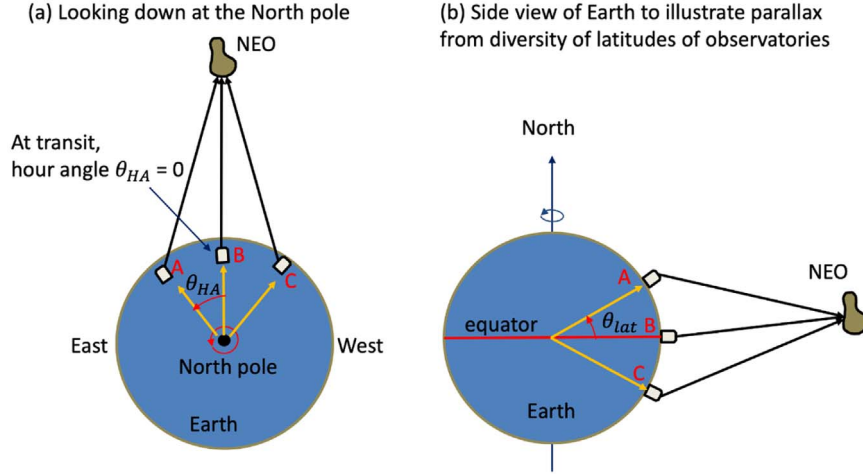


Figure 8. Schematics for illustrating parallax signals from the diversity of hour angles (left) and diversity of latitudes of observatories (right).

with same hour angles at B, B, B, or A, A, A as shown in the left plot in Figure 8, there would not be any parallax signals.

Even we schedule with hour angles as A, B, and C, the parallax that is nonlinear with time would be still small because $\sin \theta_{HA}$ is linear with time. Scheduling with hour angles alternating between A and C, such as a sequence of A, C, A, \dots , would produce much larger parallax signals. In general, we would like to swing back and forth between large positive and negative hour angles. A large hour angle would mean a high airmass. There is a trade between parallax amplitude and potentially poor measurements of high airmass. In our simulation, we required airmass to be less than 2, which would limit the parallax by a factor of $\sin 60^\circ \sim 0.875$.

We use the Monte Carlo method to generate 100 randomly scheduled observations to introduce different amplitudes of parallax for each of the 5969 close approach observation scenarios. We compute the orbit uncertainties and study the effect of parallax. The left plot in Figure 9 shows the dependency of the statistics of uncertainties of the semimajor axis estimated using 6 astrometric measurements of accuracy of 20 mas as functions of parallax Π_{HA} for regime $T\Delta < 1$ day au, where different Π_{HA} values come from the 100 random scheduling. We see an approximate linear dependency when $\Pi_{HA} > 0.35$, showing the decrease of uncertainties of orbit with Π_{HA} . For small Π_{HA} , the uncertainties do not increase as $1/\Pi_{HA}$ (the dashed gray line). This is because, for small Π_{HA} , the parallax signal is much weaker due to the corresponding scheduling of observation having less diversity of hour angles, the gravitational acceleration helps orbit determination even though $T\Delta < 1$ day au. The right plot in Figure 9 shows uncertainty statistics of the semimajor axis in the regime of $T\Delta > 1$ day au, the dependency of the orbital uncertainties on Π_{HA} is benign.

3.3.2. Parallax from Asynchronous Measurements from Multiple Observatories

We performed more simulations and linear analyses to study simultaneously having diversities of hour angles and latitudes of observatories. We let the observatories be located with respect to the location of Table Mountain with an offset latitude angle along the meridian line by a number randomly chosen from $[-60, -50, -40, -30, -20, -10, 0, 10, 20, 30]$ deg. The diversity of locations of observatories provides parallax from the change of latitudes as shown in the right plot in Figure 8, where three observatories are observing a NEO during transit. The diversity of latitudes introduce an extra astrometric signal along DEC. We similarly define Π_{lat} as a measure of contribution to the parallax signal from the diversity of latitudes $\text{lat}(t_i)$'s at t_i :

$$\Pi_{lat} \equiv \sqrt{\frac{1}{N_{\text{obs}}} \min_{\alpha, \beta} \sum_{i=1}^{N_{\text{obs}}} [\sin \text{lat}(t_i) - \alpha - \beta t_i]^2}, \quad (21)$$

where α and β are linear fitting parameters to minimize the rms of residuals. Again, if we schedule observations by alternating between observatories at A and C (see Figure 8) would enhance parallax signals. In general, we found that the diversity of hour angles and the diversity of latitudes both contribute to the total parallax defined by Equation ((16)). The approximate $1/\Pi_{\text{tot}}$ dependency of orbit determination uncertainties on the total parallax Π_{tot} is displayed in Figure 10.

Figure 11 shows the component parallax from hour angle diversity and the diversity of the latitudes of observatories. The parallax values are displayed in squares and the approximate uniform straight lines show a linear combination $\Pi_{\text{tot}}^2 \approx 0.76\Pi_{HA}^2 + 1.08\Pi_{lat}^2$. Note that this relation is empirical for observatories located in the latitude range of $34 + [-60,$

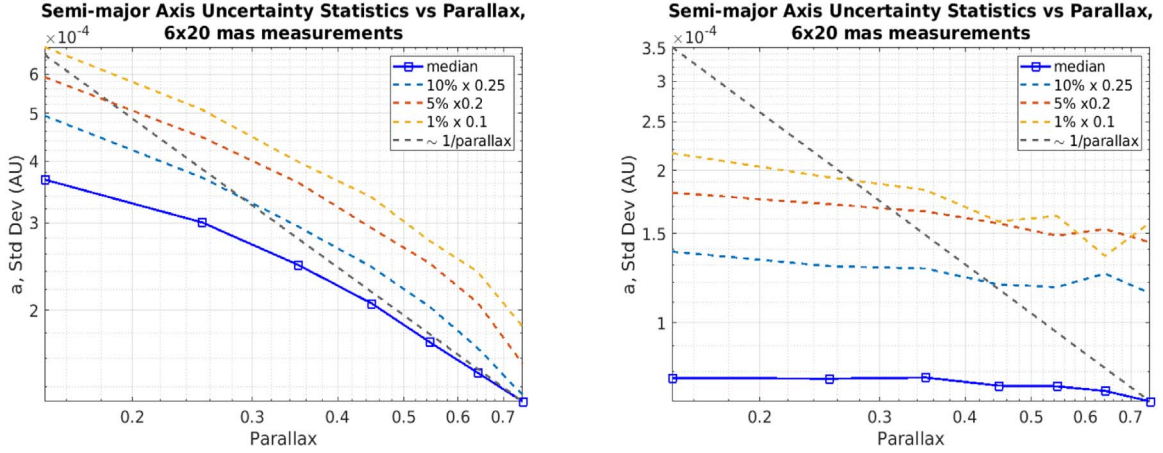


Figure 9. Semimajor axis uncertainties (1σ) statistics derived from linear analysis for using 6 astrometric measurements of accuracy 20 mas versus parallax amplitude Π_{HA} using bins of size 0.1 for parallax amplitudes. The left plot is for regime $T\Delta < 1$ day au, where the parallax signal dominates the orbit determination and the right plot is for regime $T\Delta > 1$ day au, where the gravitational acceleration signal dominates the orbit determination.

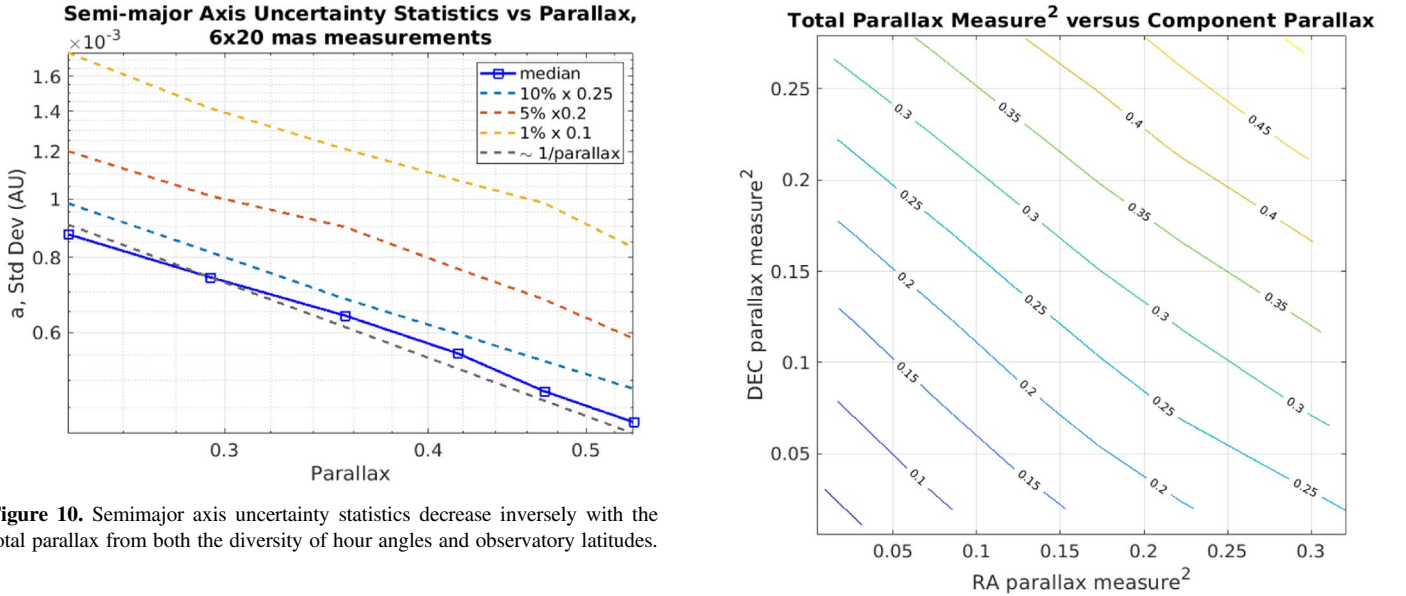


Figure 10. Semimajor axis uncertainty statistics decrease inversely with the total parallax from both the diversity of hour angles and observatory latitudes.

$30] = [-26, 64]$ deg used by our simulation. The coefficients are geometric factors from using hour angles and latitudes as coordinates on the surface of a sphere. For example, the coefficient in front of Π_{HA} is less than 1 because we did not include a cosine factor of the latitude in defining the parallax. This relation is however useful to show that we have independent contributions from diversity of hour angles and latitudes of observers. To accurately quantify the parallax, we should use Equation (16). This discussion shows that in the regime $T\Delta < 1$ day au, where parallax signal dominates the orbit determination's weak dimension, we can take the advantage of scheduling to optimize parallax as defined by Equations (20), (21), and (16) by introducing diverse hour angles and latitudes of observatories to form parallax that is

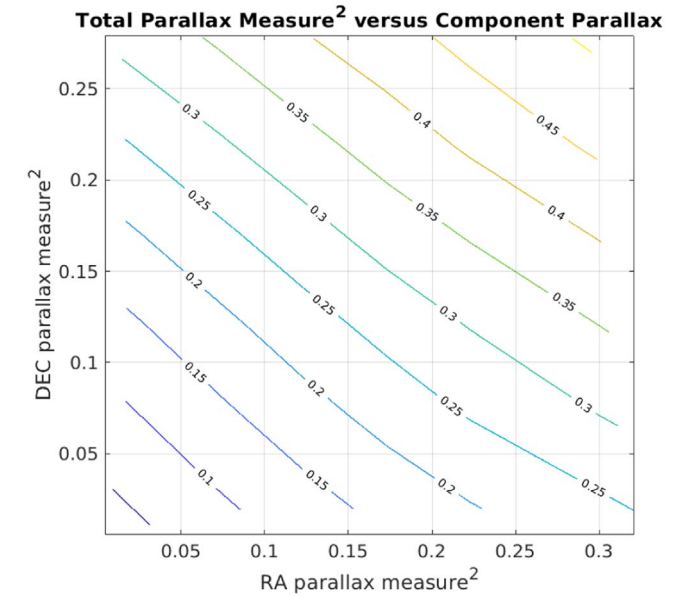


Figure 11. Contour plots showing how the component parallax from the diversity of hour angles and observatory latitudes contribute to the total parallax.

nonlinear in time. Intuitively, we should schedule observations with hour angles and latitudes alternatively between high and low values so that after a linear fit, the residuals are large.

3.3.3. Parallax from Synchronized Measurements of Two Observatories

In this subsection, we consider parallax from observations simultaneously taken by two geographically separated observatories. We use a Monte Carlo simulation to quantify the uncertainties of orbits estimated using 2 and 3 pairs of

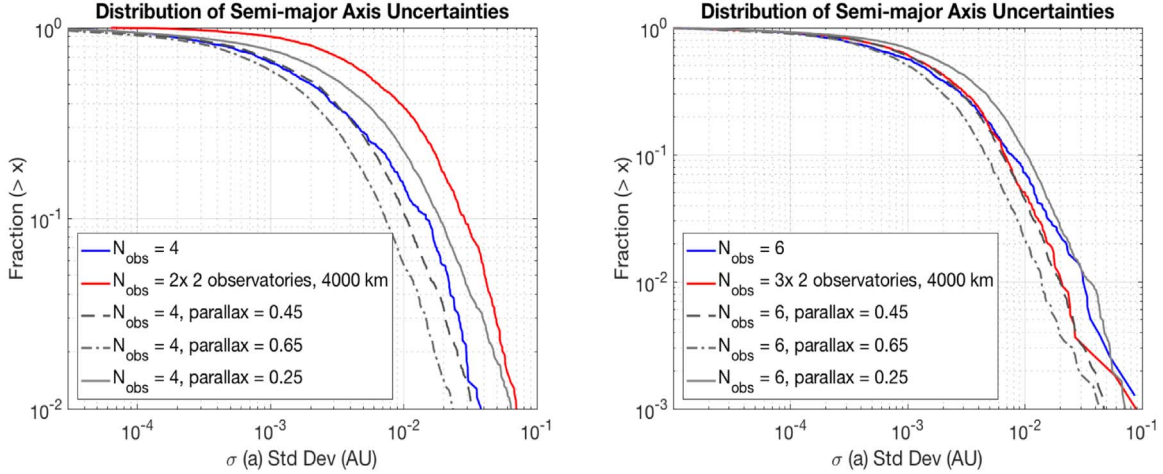


Figure 12. Comparison of semimajor axis uncertainty distribution between using two pairs of simultaneous measurements and using four measurements from a single observatory (left) and using three pairs of simultaneous measurements and using six measurements from a single observatory (right) with different amplitudes (different scheduling) of parallax from hour angle diversities.

measurements of accuracy 20 mas simultaneously taken by two observatories separated by [200, 500, 1000, 2000, 4000] km respectively. With only 2 pairs of measurements from two observatories (total four astrometric measurements), we rely on the parallax to measure the distance and radial velocity of the NEO. Only when the baseline is 2000 km or longer, we get reliable orbital solutions. The accuracy improves linearly with the length of the baseline.

The left plot in Figure 12 displays the distributions of uncertainties of semimajor axis estimated by using: (1) using two pairs of measurements at two epochs with each pair taken simultaneously by two observatories separated by 4000 km; and (2) using four randomly scheduled measurements at different epochs from a single observatory. Four measurements at different epochs (solid blue curve) have better performance than just two pairs of observations from two observatories (solid red) with a 4000 km baseline. On the same plot, we also show the distribution of uncertainties for the parallax amplitudes of 0.25, 0.45, and 0.65 respectively⁸ using four measurements of 20 mas accuracy. The blue curve, without optimizing observation schedules to maximize the parallax, approximately agrees with the parallax amplitude of $\Pi_{\text{HA}} = 0.45$. Parallax amplitude of 0.65 represents some optimization in the diversity of hour angles. In addition, it is also possible to increase parallax signals by having diversity in the latitudes of observatories.

While two paired observations do not perform as well as four measurements at different epochs, three paired measurements from a 4000 km baseline are comparable with six

measurements taken at different epochs. The right plot in Figure 12 shows the comparison of orbit uncertainties estimated using: (1) 3 pairs of simultaneous measurements, from two observatories separated by 4000 km taken at three different epochs; and (2) with 6 measurements from a single observatory taken at different epochs, both with 20 mas accuracy. The blue curve (for 6 measurements from a single observatory) crossed the red curve (for 3 paired measurements from two observatories with a baseline of 4000 km) at the large uncertainty side at fraction ~ 0.2 and $\sigma(a) \sim 4e-3$ au. This means that in about 80% of the cases, the orbital determination accuracy is better with 6 observations taken at different epochs than 3 paired observations at three epochs. However, with parallax from 4000 km baseline, using 3 paired observations has less chance to produce orbit with semimajor axis having standard deviations larger than $4e-3$ au than using 6 observations from a single observatory if scheduled with small diversities of hour angles. We also show the distribution of orbit uncertainties for parallax $\Pi_{\text{HA}} = 0.25$, 0.45, and 0.65 respectively. We find that 0.45 parallax amplitude is comparable with observing NEO using paired measurements from two observatories separated by 4000 km to form parallax. By scheduling the observations with larger parallax amplitude (0.65, for example) given by Equation (20), we can achieve better sensitivity. We can also consider baselines longer than 4000 km to improve the parallax signal formed from paired observations. This comparison shows that there seems to be no clear advantage for using paired observations from two observatories simultaneously over observations from a single observatory if we can schedule the observations with sufficient parallax amplitude. This is consistent with a similar finding was reported by Veres et al. (2014). However, when the time window of observation is only a few hours within a night, it

⁸ For each close approach scenario, we scheduled randomly 100 observations to generate the diversity of parallax, and 0.25, 0.45, and 0.65 represent respectively the cases when the amplitudes of the parallax are in bins, [0.2, 0.3], [0.4, 0.5], and [0.6, 0.7].

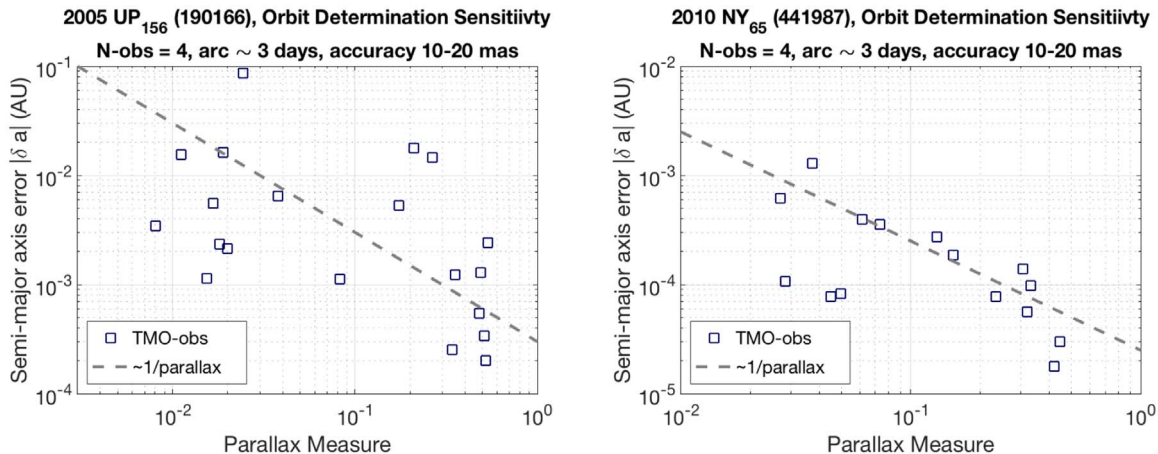


Figure 13. Orbit determination errors decreases with parallax Π_{HA} for two well observed NEOs (left, 2005UP₁₅₆, right 2010NY₆₅) to show consistently parallax signals improve orbit determination.

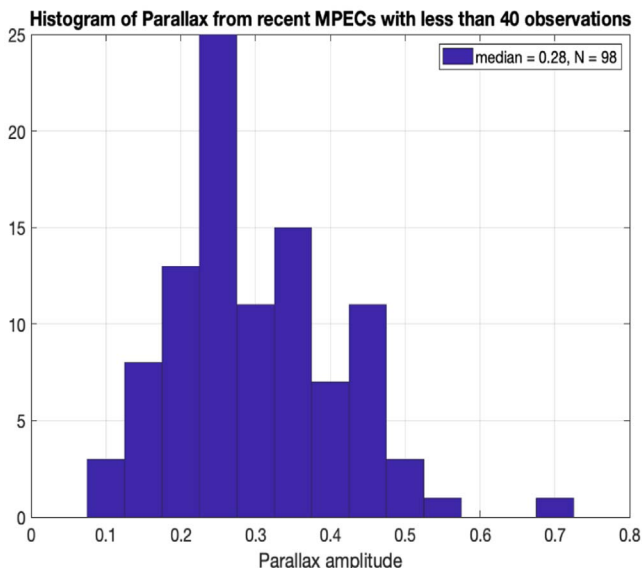


Figure 14. Histogram of Parallax Amplitudes of Recently Discovered NEOs Derived from the Observations Reported in the MPECs.

would be preferred if we have multiple observations from different observatories because the earth rotation over a few hours may not be able to introduce a significant parallax signal. In general, diversity in the observatory locations would introduce parallax to improve NEO orbit determination during a close approach, but requiring a simultaneous observation seems to be unnecessary.

3.3.4. Example of Parallax Effect Derived from Single Station Data

We have many observations of 10-20 mas accuracy from TMO 654 for asteroids 2010 NY₆₅ (441987) and 2005 UP₁₅₆

(190166). Using the online tool *Find_Orb*, we obtain different estimates of orbital parameters for different subsets of four measurements. These two asteroids are numbered objects, so we assume the orbital parameters from the JPL Horizons System (<https://ssd.jpl.nasa.gov/horizons.cgi>) to be the truth orbit for estimating orbit errors. Figure 13 shows the semimajor axis errors as a function of the parallax Π_{HA} as computed by Equation (20). The observation of 2010 NY₆₅ were taken three days after the close approach at $\Delta \sim 0.02$ au on 2017 June 24. And 2005 UP₁₅₆ was observed during the close approach ($\Delta \sim 0.13$ au) in 2017 June. We can easily see the inverse relation in Figure 13.

4. Conclusions and Discussions

We have studied the role of parallax in NEO initial orbit determination. The orbit is weakly determined because the arc length is much shorter than the NEO orbital period. The weakly determined orbit has large uncertainties in ranging the NEO, which is inferred from the nonlinear motion of the NEO in time relative to the observer. The nonlinear motion comes from the DSGA of the NEO relative to the Earth plus the topocentric parallax of observing the NEO from different positions on the Earth's surface relative to the Earth center. For NEOs during close approaches with Δ much smaller than 1 au, the relative importance of the DSGA to the parallax is quantified by the product $(T/\text{day})(\Delta/\text{au})$. When the arc length is relatively long so that $T\Delta \gtrsim 1$ day au, the DSGA dominates the orbit determination with orbit uncertainties depending on arc length as T^{-2} . For short arcs with $T\Delta \lesssim 1$ day au, the parallax dominates the determination of the NEO distance. The orbital element uncertainties are proportional to the distance of close-approach Δ .

When the arc length T is short in regime of $T\Delta \lesssim 1$ day au, which is the case for most of the newly discovered small NEOs, the orbit determination improves linearly with the parallax.

Parallax can be measured by observations from more than one observatory as well as observations from a single observatory if scheduled with diverse hour angles. In general, we want to schedule observations with the least of airmass near the transit time of the NEO. This, however, would minimize the parallax signal, which is not desired in regime $T\Delta \lesssim 1$ day au. Therefore we should trade some airmass for diverse hour angles to increase the parallax signal. One way to deal with this is to restrict the airmass to a threshold, for example, 2, and then within this limit, we will try to introduce a diversity of hour angles to increase the parallax signal. In general, alternating between large positive and negative hour angles would increase parallax amplitudes. To maximize the parallax, we should introduce both diversities of hour angles of observations and diversities of observatory latitudes because they both contribute to the total parallax signal independently. Parallax signals can be also achieved by having paired observations simultaneously from two observatories. We found that, in general, there is no specific advantage for having the measurements taken at the same time. However, a long baseline formed by two or more observatories is useful if the time window of observation is only a few hours, and the parallax signal introduced by the Earth rotation is small compared with the separation of the observatories. This situation, however, is uncommon.

Most of the newly discovered NEOs are smaller than 100 m. Small NEOs are only discovered when they are close to the Earth, therefore the parallax signal dominates the initial orbit determination. These small NEOs tend to move fast, leading to streaked images and thus suffer the trailing loss in signal-to-noise ratio and render the atmospheric effect not common between target and reference stars. Synthetic tracking (ST) technique (Shao et al. 2014; Zhai et al. 2014) can significantly improve astrometry for fast-moving NEOs by avoiding trailing loss to use CMOS cameras to take multiple short exposure frames and integrate these short exposure frames in post-processing to track both the target and reference stars. When not limited by photon noises, our NEO astrometry using ST has an accuracy of 10–20 mas. We have used images taken by an Andor’s Zyla 5.5 CMOS camera on the Pomona College’s 40 inch telescope to achieve 10 mas NEO astrometry comparable with the accuracy of stellar astrometry (Zhai et al. 2018). Note that this accuracy does not degrade with the increase of the rate of the motion, very suitable for observing NEOs at the closest approach.

Figure 14 shows the histogram of parallax amplitudes for 98 recently discovered NEOs from 2021 October to early 2021 November. The parallax amplitudes are computed using the observational data reported in the MPECs. We only considered the cases where the number of observations is less than 40. The median value is 0.28. If we schedule randomly, the median value of Π_{HA} from the diversity of hour angles is ~ 0.45 , giving a parallax amplitude ~ 0.37 at latitude 34° . This means that there is room to improve parallax amplitudes.

We recommend using ST to observe NEOs when they are close to the Earth to produce accurate astrometry and optimizing the parallax by introducing a cadence of observations to alternate between large positive and negative hour angles (allowed by air mass limit) as well as high and low latitudes of observatories so that the nonlinear portion of parallax with time is large. We expect ST to play a significant role in improving the accuracy of initial orbit for small NEOs with short arcs.

We thank Bill Owen, who retired from JPL, and Stuart Shaklan at JPL for many insightful discussions and advice. We appreciate the instrumentation support from Heath Rhoades at JPL as well as Tony Grigsby and Hardy Richardson at Pomona College. We also thank the anonymous reviewer for helping improve the manuscript. The work was supported by JPL’s internal research fund and NASA ROSES YORPD program. This work has made use of data from the European Space Agency (ESA) mission Gaia (<https://www.cosmos.esa.int/gaia>), processed by the Gaia Data Processing and Analysis Consortium (DPAC, <https://www.cosmos.esa.int/web/gaia/dpac/consortium>). Funding for the DPAC has been provided by national institutions, in particular the institutions participating in the Gaia Multilateral Agreement. The research was carried out at the Jet Propulsion Laboratory, California Institute of Technology, under a contract with the National Aeronautics and Space Administration (80NM0018D0004).

Appendix Derivations

In this appendix, we derive Equations (6) and (7) in Section 2.1 and Equation (10) in Section 2.2. Recall the definitions (5) for a right hand orthonormal basis ($\hat{\rho}_e$, $\hat{\nu}$, \hat{n}) using the unit vector $\hat{\rho}_e(t)$ and the first derivative $\dot{\hat{\rho}}_e$ as

$$\eta \equiv |\dot{\hat{\rho}}_e(t)|, \quad \hat{\nu} \equiv \dot{\hat{\rho}}_e(t)/\eta, \quad \hat{n} \equiv \hat{\rho}_e(t) \times \hat{\nu}, \quad (\text{A1})$$

where the orthogonality between $\hat{\rho}_e$ and $\hat{\nu}$ follows from the fact that

$$\frac{d}{dt}(\hat{\rho}_e \cdot \hat{\rho}_e) = 2\frac{d\hat{\rho}_e}{dt} \cdot \hat{\rho}_e \equiv 2\dot{\hat{\rho}}_e \cdot \hat{\rho}_e = 2\eta\hat{\rho}_e \cdot \hat{\nu} = 0. \quad (\text{A2})$$

By the same argument, we have $\dot{\hat{\nu}} \cdot \hat{\nu} = 0$. Taking derivative of $\hat{\rho}_e \cdot \hat{\nu} = 0$ gives

$$\begin{aligned} \frac{d}{dt}(\hat{\nu} \cdot \hat{\rho}_e) &= \dot{\hat{\nu}} \cdot \hat{\rho}_e + \hat{\nu} \cdot \dot{\hat{\rho}}_e \\ &= \dot{\hat{\nu}} \cdot \hat{\rho}_e + \hat{\nu} \cdot \eta\hat{\nu} = \dot{\hat{\nu}} \cdot \hat{\rho}_e + \eta = 0 \end{aligned} \quad (\text{A3})$$

Using $\dot{\hat{\nu}} \cdot \hat{\nu} = 0$ and with the projection to $\dot{\hat{\nu}} \cdot \hat{\rho}_e = -\eta$, we can write

$$\dot{\hat{\nu}} = -\eta \hat{\rho}_e + \kappa\eta \hat{n} \quad (\text{A4})$$

where scalar κ measures the rate for the motion deviates from a great circle (the geodesic curvature, see Milani et al. (2008)).

Therefore,

$$\ddot{\hat{\rho}}_e = \frac{d(\eta \hat{\nu})}{dt} = -\eta^2 \hat{\rho}_e + \dot{\eta} \hat{\nu} + \kappa \eta^2 \hat{n}. \quad (\text{A5})$$

which is Equation (6). Taking two derivatives with respect to time t of $\rho_e(t) = \rho_e(t) \hat{\rho}_e(t)$, we get Equation (7) as the following:

$$\begin{aligned} \ddot{\rho}_e(t) &= \ddot{\rho}_e(t) \hat{\rho}_e(t) + 2\dot{\rho}_e(t) \dot{\hat{\rho}}_e(t) + \rho_e(t) \ddot{\hat{\rho}}_e(t) \\ &= \ddot{\rho}_e(t) \hat{\rho}_e(t) + 2\dot{\rho}_e(t) \eta \hat{\nu} + \rho_e(t) (\dot{\eta} \hat{\nu} - \eta^2 \hat{\rho}_e + \kappa \eta^2 \hat{n}) \\ &= (\ddot{\rho}_e(t) - \eta^2) \hat{\rho}_e(t) + (2\dot{\rho}_e \eta + \rho_e \dot{\eta}) \hat{\nu} + \kappa \eta^2 \rho_e \hat{n}. \end{aligned} \quad (\text{A6})$$

We now turn to derive Equation (10) in Section 2.2. NEO observations are usually performed when the NEO is close to the Earth, therefore, we have $\rho \sim \rho_e \ll q_e \sim 1$ au in general. Starting with Equation (9), we expand it in powers of ρ_e/q_e and keep terms up to $(\rho_e/q_e)^2$ to get

$$\begin{aligned} \ddot{\rho}_e &= -\mu \left[\frac{q_e + \rho_e}{(q_e^2 + 2q_e \cdot \rho_e + \rho_e^2)^{3/2}} - \frac{q_e}{q_e^3} \right] \\ &= -\mu \left[\frac{q_e}{(q_e^2 + 2q_e \cdot \rho_e + \rho_e^2)^{3/2}} - \frac{q_e}{q_e^3} \right] \\ &\quad - \mu \frac{\rho_e}{(q_e^2 + 2q_e \cdot \rho_e + \rho_e^2)^{3/2}} \\ &= -\mu \frac{q_e}{q_e^3} \left[\left(1 + \frac{2q_e \cdot \rho_e + \rho_e^2}{q_e^2} \right)^{-3/2} - 1 \right] \\ &\quad - \mu \frac{\rho_e}{q_e^2} \left(1 + \frac{2q_e \cdot \rho_e + \rho_e^2}{q_e^2} \right)^{-3/2} \\ &\approx -\mu \frac{q_e}{q_e^3} \left[-\frac{3}{2} \frac{2q_e \cdot \rho_e + \rho_e^2}{q_e^2} + \frac{15}{8} \left(\frac{2q_e \cdot \rho_e + \rho_e^2}{q_e^2} \right)^2 \right] \\ &\quad - \mu \frac{\rho_e}{q_e^3} \left(1 - \frac{3}{2} \frac{2q_e \cdot \rho_e + \rho_e^2}{q_e^2} \right) \\ &\approx -\mu \frac{q_e}{q_e^3} \left[-\frac{6q_e \cdot \rho_e + 3\rho_e^2}{2q_e^2} + \frac{15}{8} \frac{(2q_e \cdot \rho_e)^2}{q_e^4} \right] \\ &\quad - \mu \frac{\rho_e}{q_e^3} \left(1 - \frac{3}{2} \frac{2q_e \cdot \rho_e}{q_e^2} \right) \\ &= -\mu \frac{q_e}{q_e^3} \left[-\frac{6q_e \cdot \rho_e + 3\rho_e^2}{2q_e^2} + \frac{(15q_e \cdot \rho_e)^2}{2q_e^4} \right] \\ &\quad - \mu \frac{\rho_e}{q_e^3} \left(1 - \frac{3q_e \cdot \rho_e}{q_e^2} \right), \end{aligned} \quad (\text{A7})$$

where we have used

$$(1+x)^{-3/2} = 1 - \frac{3}{2}x + \frac{15}{8}x^2 + O(x^3). \quad (\text{A8})$$

For astrometric signal, we are only interested in the component that is perpendicular to $\hat{\rho}_e$, therefore, the second term in Equation (A7) does not contribute. We obtain

$$\begin{aligned} [\ddot{\rho}_e]_{\perp} &\approx -\mu \left[\frac{q_e}{q_e^3} \right]_{\perp} \left[-\frac{6q_e \cdot \rho_e + 3\rho_e^2}{2q_e^2} + \frac{(15q_e \cdot \rho_e)^2}{2q_e^4} \right] \\ &= \frac{3\mu}{q_e^3} \left[\frac{2q_e \cdot \rho_e + \rho_e^2}{2q_e^2} - \frac{5(\hat{q}_e \cdot \rho_e)^2}{2q_e^2} \right] [q_e]_{\perp} \\ &= \frac{3\mu}{q_e^3} \left[\frac{\hat{q}_e \cdot \rho_e}{q_e} + \frac{\rho_e^2 - 5(\hat{q}_e \cdot \rho_e)^2}{2q_e^2} \right] [q_e]_{\perp} \end{aligned} \quad (\text{A9})$$

which provides the derivation of Equation (10).

ORCID iDs

Chengxing Zhai  <https://orcid.org/0000-0002-0291-4522>

References

- Bellm, E. C., Kulkarni, S. R., Graham, M. J., et al. 2019, *PASP*, **131**, 018002
 Bernstein, & Kushalani 2000, *AJ*, **120**, 3323
 Buie, M. W., et al. 2016, *AJ*, **152**, 122, 23pp
 Christensen, E. J. 2019, in *Planetary Defense Conf.*, ed. W. Ailor (Washington, DC: AA)
 Danby, J. M. A. 1988, *Fundamentals of Celestial Mechanics* (Second edn.; Richmond, VA: Willmann Bell)
 Duev, D. A., Mahabal, A., Ye, Q., et al. 2019, *MNRAS*, **486**, 4158
 Farnocchia, D., et al. 2015, *Icar*, **245**, 94, arXiv:1407.8317
 Fletcher, R. 1987, *Practical Methods of Optimization* (Second edn.; New York: Wiley), **111**, Chapter 6
 Granvik, M., et al. 2016, *Natur*, **530**, 303
 Heinze, A., Metchev, S., & Trollo, J. 2015, *AJ*, **150**, 125
 Ivezić, Z., Kahn, S. M., Tyson, J. A., et al. 2019, *ApJ*, **873**, 111
 Kaiser, N., Aussel, H., Burke, B. E., et al. 2002, *Proc. SPIE*, **4836**, 154
 Lin, et al. 2016, *AJ*, **152**, 183
 Luenberger, D. G. 1969, *Optimization by Vector Space Methods* (New York: Wiley)
 Mainzer, A., Grav, T., Bauer, J., et al. 2015, *AJ*, **149**, 172
 Marchi, S., Momany, Y., & Bedin, L. R. 2004, *NewA*, **9**, 679
 Metchev, Heinze 2015, *AJ*, **150**, 124
 Milani, et al. 2005, *Icar*, **179**, 350
 Milani, et al. 2008, *Icar*, **195**, 474
 Poincare, H. 1906, *BuAst*, **23**, 161
 Roa, J., Farnocchia, D., Chodas, P. W., et al. 2020, *AJ*, **160**, 250, 12 pp
 Shao, M., Nemati, B., Zhai, C., et al. 2014, *ApJ*, **782**, 1
 Tonry, J., et al. 2018, *PASP*, **139**, 478
 Vereš, P., Farnocchia, D., Chesley, S., & Chamberlin, A. B. 2017, *Icar*, **296**, 139
 Vereš, P., Farnocchia, D., Jedicke, R., & Spoto, F. 2014, The effect of parallax and cadence on asteroid impact probabilities and warning times, 2014, *PASP*, **126**, 433
 Vereš, P., Payne, M. J., Holman, M. J., et al. 2018, *Unconfirmed Near-Earth Objects*, *AJ*, **156**, 5
 Ye, Q., et al. 2019, *PASP*, **131**, p078002
 Zhai, C., Shao, M., Nemati, B., et al. 2014, *ApJ*, **792**, 60
 Zhai, C., Shao, M., Saini, N. S., et al. 2018, *AJ*, **156**, 65